A Hot Gap Around Jupiter's Orbit in the Solar Nebula

N. J. Turner, M. Choukroun, J. Castillo-Rogez and G. Bryden

Jet Propulsion Laboratory, California Institute of Technology, Pasadena, California 91109, USA; neal.turner@jpl.nasa.gov

ABSTRACT

The Sun was an order of magnitude more luminous during the first few hundred thousand years of its existence, due in part to the gravitational energy released by material accreting from the Solar nebula. If Jupiter was already near its present mass, the planet's tides opened an optically-thin gap in the nebula. We show using Monte Carlo radiative transfer calculations that sunlight absorbed by the nebula and re-radiated into the gap raised temperatures well above the sublimation threshold for water ice, with potentially drastic consequences for the icy bodies in Jupiter's feeding zone. Bodies up to a meter in size were vaporized within a single orbit if the planet was near its present location during this early epoch. Dust particles lost their ice mantles, and planetesimals were partially to fully devolatilized, depending on their size. Scenarios in which Jupiter formed promptly, such as those involving a gravitational instability of the massive early nebula, must cope with the high temperatures. Enriching Jupiter in the noble gases through delivery trapped in clathrate hydrates will be more difficult, but might be achieved by either forming the planet much further from the star, or capturing planetesimals at later epochs. The hot gap resulting from an early origin for Jupiter also would affect the surface compositions of any primordial Trojan asteroids.

Subject headings: protoplanetary disks — radiative transfer

1. INTRODUCTION

The Sun was more luminous when very young (Hayashi 1961; D'Antona & Mazzitelli 1994; Siess et al. 2000) and it is natural to ask about the consequences for planet formation. Sunlight was the main heat source for the outer parts of the protosolar nebula (Dullemond

et al. 2007), so the Solar luminosity surely affected the distribution of ices. Water ice was the most abundant solid in locations where the temperatures were below its sublimation threshold (Pollack et al. 1994; Dodson-Robinson et al. 2009b) and played a key role in the assembly of the outer planets, their moons, the Kuiper belt objects and the comets, judging from the bodies' compositions. Water ice is invoked as a major building block for the solid cores of the gas giant planets, whether the cores were built before (Pollack et al. 1996) or after (Helled & Schubert 2009) the gaseous envelopes. Water ice also is used to explain Jupiter's atmospheric enrichment in the noble gases argon, krypton and xenon relative to the Sun (Young 2003). Volatile species including the noble gases can be trapped in amorphous ice forming at temperatures below about 30 K (Owen et al. 1999) and in clathrate hydrates at somewhat higher temperatures (Lunine & Stevenson 1985; Hersant et al. 2004). Extra motivation for examining the delivery of ices to Jupiter is the prospect of better composition and internal structure measurements after the Juno spacecraft reaches the planet in 2016 (Bolton 2010).

In this paper we focus on the consequences of the Sun's higher early luminosity for material close to Jupiter. Ideas about Jupiter's origins fall into two main groups. In core-nucleated accretion models, a solid core of ice and rock accumulates over one to several million years before a significant gaseous envelope is accreted (Pollack et al. 1996; Hubickyj et al. 2005; Movshovitz et al. 2010). In gravitational instability models, the Solar nebula at some time during its first few hundred thousand years is sufficiently massive to fragment locally under its own self-gravity. Jupiter forms within a thousand years from one of the fragments (Boss 1997; Durisen et al. 2007). The two groups of models thus differ drastically in the epoch when the planet approaches its final mass.

When applied to the exoplanet population, core-nucleated accretion more easily explains the formation of the gas giants with massive cores (Sato et al. 2005), while gravitational instability can account for the formation of high-mass exoplanets found far from their host stars (Dodson-Robinson et al. 2009a; Cai et al. 2010).

Once formed, Jupiter is sufficiently massive that its tides open a gap in the Solar nebula (Lin & Papaloizou 1986, 1993). The reduced surface density in the gap may allow sunlight to penetrate to the equatorial plane, either through scattering, or absorption in the nebula and re-radiation. Only in the gravitational instability scenarios does Jupiter become massive enough to open such a gap in the nebula while the Sun is still much more luminous than today. Our goal is to evaluate the impact of the high luminosity on the planet and its surroundings.

Below, we compute the temperatures reached in the nebula and gap under thermal equilibrium with the radiation from the protosun. Similar radiative transfer calculations

by Varnière et al. (2006) revealed that owing to the protostellar disk's concave or flared surface, the outer edge of the gap intercepts an excess of starlight, and appears as a bright ring in synthetic scattered light images. Varnière et al. (2006) presented results with a fixed power-law radial variation in the density scale height, and stated that the outcome was similar under hydrostatic equilibrium. Their central sun had about $1.4L_\odot$, corresponding to a T Tauri star of age 1–3 Myr. In contrast, our models all are in hydrostatic balance, and we consider a protostar aged less than 0.3 Myr with ten times the Solar luminosity, appropriate for the early epoch of planet formation in the gravitational instability picture. We find that the more-luminous sun heats the gap enough to destroy many volatiles in the vicinity of the planet.

The paper is laid out as follows. The models for the protosun and nebula are described in sections 2.1 and 2.2, the radiative transfer approach in section 2.3 and the iterative method used to obtain joint radiative and hydrostatic equilibrium in section 2.4. The equilibrium results are presented in section 3, the location and extent of the heating and the effects on ices discussed in section 4, and the implications for gas giant planet formation summarized in section 5.

2. METHODS

2.1. The Sun

Solar-mass protostars are larger, cooler and more luminous than the Sun today, according to classical stellar evolution modeling. The modeling assumes spherical collapse from some arbitrary large initial radius, with the mass fixed. The protostar maintains approximately constant surface temperature over its first million years, while shrinking as convection transports the heat of contraction to the surface where it is radiated away (Hayashi 1961). From "birth" when the protostar first becomes visible in the infrared, the luminosity decreases by about an order of magnitude before the central temperature increases enough for the onset of hydrogen fusion. The intrinsic luminosity from contraction and nucleosynthesis exceeds $10L_\odot$ for the first $2–3 \times 10^5$ years (figure 1).

The protosun's surroundings were in fact far from spherically symmetric. Owing to the difficulty of extracting the angular momentum from the birth cloud, the material that eventually accreted on the Sun mostly passed first through the rotation-supported Solar nebula. Much of the gravitational energy released in forming the nebula was radiated away before the gas reached the star. In the limit where all the energy escaped, called cold accretion, the protosolar radius was significantly smaller (Hartmann et al. 1997). However if
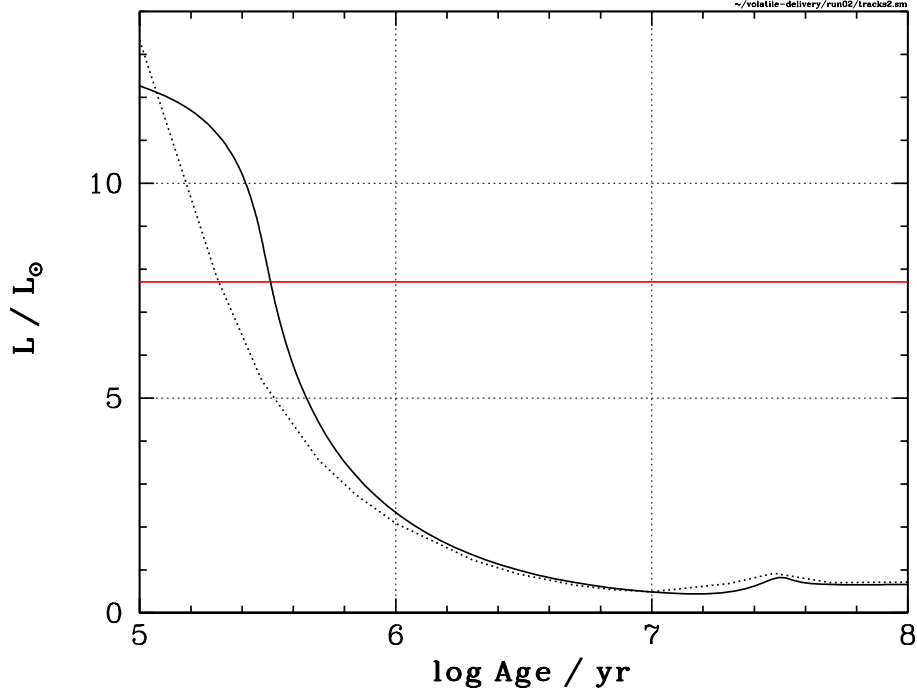
Fig. 1.— Luminosity vs. time in two models for the evolution of a Solar-mass protostar. The dotted curve is from D'Antona & Mazzitelli (1994), the solid curve from Siess et al. (2000). Both models include nuclear fusion and the heat of contraction, but fix the stellar mass and neglect the energy released by ongoing accretion. A horizontal red line shows the power released in accreting 10^{-6} M$_\odot$ yr^{-1} on a Solar-mass protostar of radius 2 $R_\odot$. Growing to near Solar mass in a million years required the young Sun to reach total luminosities similar to or greater than ten times the modern value.

even a small fraction of the released energy was carried into the protostar with the accreting material, the protosun was larger and hotter (Hosokawa et al. 2011; Hartmann et al. 2011).

In addition to the intrinsic luminosity, protostars shine with the energy released during the accretion. Growing a Solar-mass star in a million years requires an average accretion rate of $10^{-6} M_\odot \mathrm{yr}^{-1}$. The rate of gravitational energy release near the end of the growth is $8 L_\odot$ if the accreted material is deposited on the surface of a star with radius $2R_\odot$. If the accretion is unsteady, the peak luminosities will be higher still.

Empirical stellar temperatures and luminosities are available for some protostars that have built up much of their mass but are still accreting gas from their birth cloud. Near-infrared absorption lines formed close to the stellar photosphere can be observed despite the

high circumstellar extinction. An example is YLW 15. Modeling of its spectrum indicates the bolometric luminosity $10L_\odot$ is made up of $3L_\odot$ from the star's internal power sources and $7L_\odot$ from mass accretion at a rate $1.6 \times 10^{-6} M_\odot \, \mathrm{yr}^{-1}$. The protostar has mass $0.5M_\odot$ and radius $3.1R_\odot$ (Greene & Lada 2002). Similar results were obtained for larger samples by Nisini et al. (2005) and Doppmann et al. (2005). Evans et al. (2009) derived from SPITZER photometry an overall protostellar luminosity function for five nearby star-forming regions. The sample in their figure 14 has a median mass well below a Solar mass, and includes objects aged up to about 0.54 Myr, two to three times the length of the high-luminosity epoch shown in figure 1 above. Nevertheless a substantial minority have extinction-corrected bolometric luminosities $10L_\odot$ and above.

Considering the intrinsic and accretion luminosities together, we conclude that the Sun's total output exceeded $10L_\odot$ for at least part of the Solar system's first million years. We investigate the consequences of the high early Solar luminosity for temperatures in the surrounding nebula. Given the uncertainties regarding the protosolar radius and temperature, it is appropriate to consider ranges in these parameters. As representative examples we choose two model protosuns. Both are spherical blackbody radiators of mass $1M_\odot$ and luminosity $10L_\odot$. Star [A] has radius $5R_\odot$ and temperature $4\,600$ K, while star [B] has radius $2R_\odot$ and temperature $7\,290$ K.

2.2. The Solar Nebula

Measurements using interferometers at sub-millimeter wavelengths show that protostellar disks have dust surface densities falling off approximately inversely with radius R outside 30 AU, the smallest scale resolved in nearby star-forming regions (Andrews et al. 2010). The distribution of material nearer the star has few direct observational constraints. For the first of three Solar nebula models, we therefore choose a surface density $\propto 1/R$, normalized so that the outer parts are unstable according to the Toomre criterion $Q < 1$ (Toomre 1964; Binney & Tremaine 1987), as required to form Jupiter through a gravitational instability. The surface density is $6\,800$ g cm^{-2} at 1 AU in this model which we label [D].

As a simple case including a gap, we consider a second model [G] with an ad hoc reduction in the surface density between 3.3 and 7 AU. Away from either gap edge, the surface density declines approximately as a Gaussian with scale length 5% of the gap edge radius. A floor is also imposed so the surface density is not less than 10^{-6} times that at the same radius in model [D].

For a more detailed model of the disk and gap, we assume viscous stresses balance the

planetary tides, and the planet accretes a prescribed fraction of the material flowing past (Lubow & D'Angelo 2006). The resulting disk model [V] has viscous stress parameter $\alpha = 0.005$, planetary accretion efficiency $E = 6$, gap width parameter $f = 2$ and planet/star mass ratio $q = 1/1000$. Our planetary accretion efficiency is lower than the $E = 8$ fiducial case of Lubow & D'Angelo (2006) because we ultimately obtain a lower aspect ratio $H/r = 0.04$ near 5 AU.

Models [G] and [V] have similar gap widths at unit vertical optical depth in the starlight (figure 2), with ratios of outer to inner radius 1.31. Comparing the outcomes of the two thus helps distinguish the effects of the gap from those of the other features the planet induces in the model [V] surface density profile.

All three nebula models [D], [G] and [V] extend from 0.04 to 40 AU with a Gaussian roll-off in the surface density at the inner rim to prevent an artificially hot vertical wall facing the star. The masses of the models are 0.191, 0.176 and $0.191 M_\odot$, respectively. All three are axially symmetric, and symmetric about the equatorial plane. The Toomre Q parameter is less than unity indicating gravitational instability outside 27 AU in disks [D] and [G], and 21 AU in disk [V].

The planet Saturn is also capable of opening a gap in the Solar nebula under favorable conditions. Balancing the nebula's viscous stresses against the tides of a single Saturn-mass planet located at 10 AU, with all other parameters unchanged, we obtain an alternative version of model [V] discussed in section 4.

In the traditional Shakura-Sunyaev picture, material spiralling inward through the disk releases its gravitational energy as heat deposited locally. This accretional or viscous heating is strong enough to dominate over the stellar illumination at 5 AU for mass flow rates above about 10^{-7} $M_\odot$ yr^{-1} for T Tauri star parameters (Dullemond et al. 2007). The higher stellar luminosity we consider means that accretional heating will be important only at mass flow rates exceeding 10^{-6} $M_\odot$ yr^{-1}. Furthermore, detailed radiation-MHD calculations of the gravitational energy's release and dissipation mediated by magnetic fields indicate that most of the power is deposited at low optical depths in the disk atmosphere, rather than in the interior (Hirose & Turner 2011). We therefore neglect accretional heating, and obtain lower bounds on the temperatures by considering only the stellar illumination.

2.3. Radiative Transfer

We compute the radiative equilibrium temperatures by emitting a large number of photon packets from the star into the nebula where they are scattered, absorbed and re-
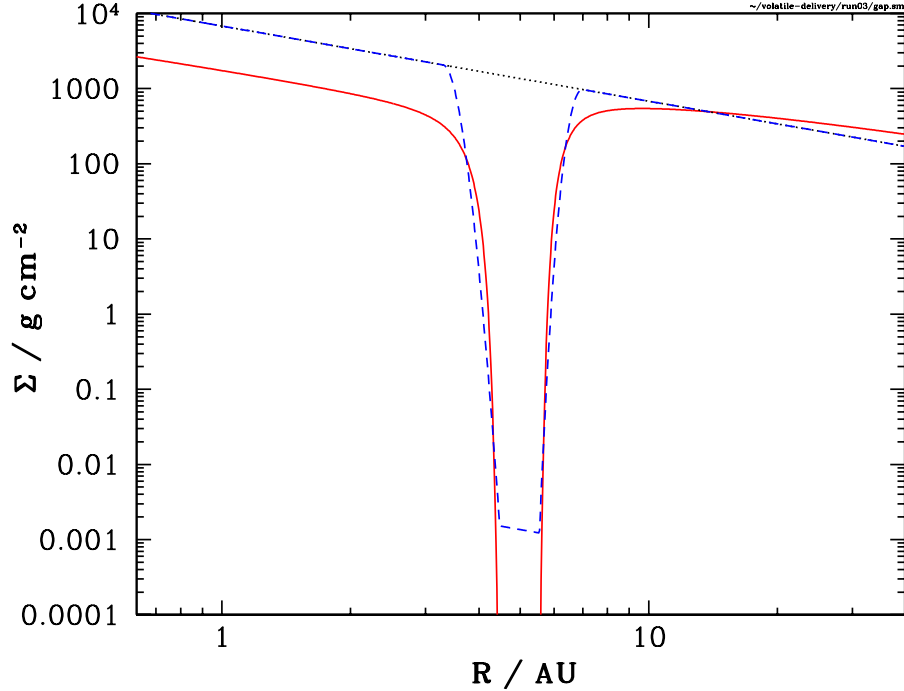
Fig. 2.— Surface density profiles of the three Solar nebula models. The simple power law model [D] is shown by a black dotted line, the power law with gap [G] by a blue dashed line, and the viscous disk plus gap model [V] by a red solid line. The viscous model is from Lubow & D'Angelo 2005 with planet-to-star mass ratio $q = 10^{-3}$, planetary accretion efficiency $E = 6$ and Shakura-Sunyaev viscosity parameter $\alpha = 0.005$.

emitted as many times as needed till they escape to infinity. With this approach the energy is conserved exactly. The stellar luminosity is divided equally among the packets. We use the temperature relaxation procedure of Bjorkman & Wood (2001), drawing the frequencies of the re-emitted packets from the difference between the old and new emission spectra, such that the local radiation field adjusts to the updated temperature. For efficiency when estimating the radiation absorption rates, we include the contributions from all along the packet paths (Lucy 1999).

The nebula's interior is isothermal on cylinders, since we neglect accretional heating. We therefore save the expense of computing temperatures in the most optically-thick regions by simply bouncing back any packets reaching a certain mass column, chosen so the overlying material is optically thick at wavelengths near its thermal emission peak. The bouncing threshold is set to 20 g cm^{-3} in all the calculations shown here. Additional tests with a

threshold of 50 g cm^{-3} gave similar results. We replace the missing interior temperatures by the mean of the last few well-sampled values above.

We adopt opacities from Preibisch et al. (1993) who matched Mie calculations of dust particles' optical response against data from molecular clouds. The grain model consists of silicate particles, mantled with water and ammonia ice that is polluted with fine carbon-rich particles. The mantles increase the particles' radii by 14.5%. At temperatures above 125 K the ice sublimates, releasing the carbon particles. Above 1 500 K the silicates also sublimate, leaving only the carbon particles. Finally, above 2 000 K the carbon particles are destroyed too. Each particle species has a power-law size distribution with exponent -3.5. The minimum and maximum sizes are 0.04 and 1 μm for the silicate particles and 0.007 and 0.03 μm for the carbon particles. The opacity curves are shown in figure 3. Scattering contributes about half of the total cross-section at optical wavelengths, and is assumed isotropic. Above 2 000 K we set the opacity to a low level of 10^{-4} g cm^{-3} representing the residual effects of molecular lines in the opacity gap at temperatures between the dust destruction and hydrogen ionization thresholds (Bell & Lin 1994). Such high temperatures are found only far from the gap, in the optically-thin material near the disk's inner rim.

The disk is divided into a grid of cells, each of which has a single uniform temperature for dust and gas. The dust is assumed to be well-mixed in the gas. The grid has 300 cells spaced logarithmically in radius R between 0.04 and 40 AU. With 100 cells per decade, each cell is 2.3% further from the star than the last. In the vertical direction, the grid has 200 cells uniformly-spaced between the equatorial plane and height $z = 0.4R$, yielding cells separated by 0.2% of the radius.

2.4.   Joint Radiative and Hydrostatic Equilibrium

Once new temperatures have been found through the Monte Carlo radiative transfer procedure, we restore vertical hydrostatic equilibrium by solving the force balance equation within each disk annulus, while holding fixed the surface density and the variation of the temperature with the column mass.

We iterate five times between radiative transfer and hydrostatic balancing. Each iteration involves 10^6 photon packets. We then use the result of the fourth iteration as the initial condition for two further iterations with 10^7 packets each, and check that the larger number of packets leaves the disk structure almost unchanged.

During the thermal relaxation procedure the opacity curves must remain fixed (Bjorkman & Wood 2001), while the opacities we use vary with temperature across the sublimation
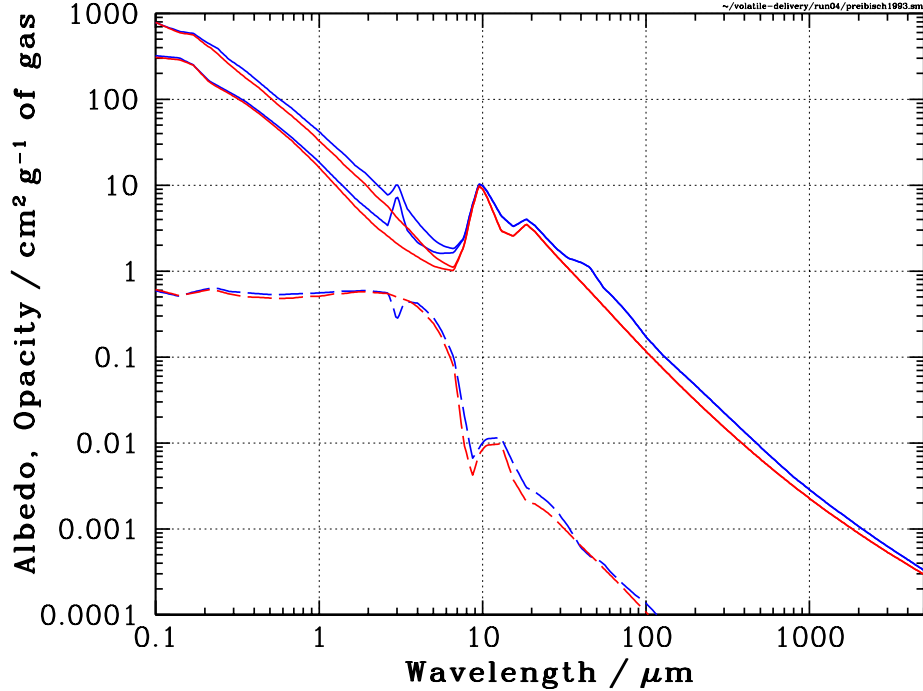
Fig. 3.— Wavelength dependence of the opacities for silicate particles, with (blue) and without (red) mantles of ice contaminated with amorphous carbon (Preibisch et al. 1993). The red curves include the opacity from the amorphous carbon particles released when the ice sublimates. The lower in each pair of solid curves shows the absorption opacity, the upper the sum of absorption and scattering opacities. Dashed curves indicate the albedos.

thresholds for water, silicates and carbon-rich grains (figure 3). Throughout each iteration we therefore set each grid cell's opacity curve according to the temperature found there on the previous iteration.

3. RESULTS

We compute temperatures in the gap for all six star-disk combinations. The six runs are listed in table 1 along with the temperatures T_p found at the planet's orbit. The temperatures in the equatorial plane are especially important for the ice distribution, since the vertical component of the Sun's gravity keeps macroscopic solid bodies lying mostly near the nebula's midplane (Weidenschilling & Cuzzi 1993). All four cases with gaps have similar temperature profiles, as do the two cases without gaps. We choose to focus on run 3 with the larger,

Table 1: The six Monte Carlo radiative transfer calculations.

Run number	Star model	Disk model	T_p (K)
1	[A]	[D]	88
2	[A]	[G]	159
3	[A]	[V]	159
4	[B]	[D]	100
5	[B]	[G]	178
6	[B]	[V]	183

cooler star [A] and viscous disk [V]. Selected results are in figures 4 to 10.

Several iterations of the radiative and hydrostatic equilibrium procedure for run 3 are shown in figure 4. The temperature is initially set to $200\,\mathrm{K}/R_{\mathrm{AU}}^{-1/2}$, approximating the final midplane temperature profile obtained in run 1. The disk is thus initially isothermal on cylinders. Its flared surface together with the absence of material from the gap means the gap's outer edge receives extra starlight. Note that the effect is exaggerated in figure 4 by the magnified vertical scale. The gap's outer edge heats and, under hydrostatic equilibrium, expands. On the next iteration, the taller outer edge intercepts yet more starlight and expands further. At the same time, the gap's inner edge receives reprocessed radiation from the outer edge and also heats and expands slightly. The changes are smaller with successive iterations, and after three iterations the gap changes little. However the disk beyond the gap's puffed-up outer edge now lies in shadow, and becomes cooler and thinner. After falling into shadow, the outer disk also rapidly converges, and between the two iterations with 10^7 packets, there is little change.

As described in section 2.4 our procedure yields two versions of the fifth iteration, one using 10^6 photon packets and another with 10^7. The differences between these two are consistent with the expected Monte Carlo noise in all six runs. Therefore from now on we discuss only the results from the version of the fifth iteration with 10^7 packets.

The paths followed by packets entering the gap are plotted in figure 5. Most of the radiation heating the gap midplane is starlight reprocessed in the outer rim, as shown by the larger number of red than blue points. The packet paths appear curved because for purposes of the plot, they are projected onto a meridional plane by rotation. Some of the packets enter the gap traveling near a tangent to the planet's orbit.
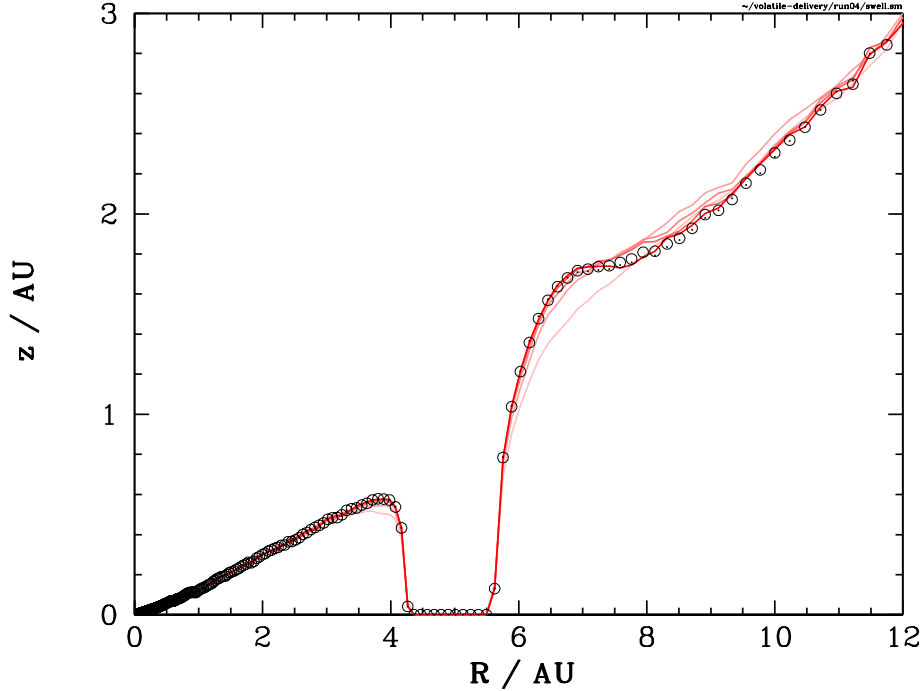
Fig. 4.— Surface of unit vertical optical depth at the wavelength of the stellar blackbody peak (0.65 μm) after one, two, three, four and five iterations of radiative and hydrostatic balancing (curves colored from pink to deep red) in run 3. Each iteration involves 10^6 photon packets. The height of the gap's outer edge near 6.5 AU increases over the first three iterations and then changes little between the last three. We also use the fourth iteration as the initial condition for two further iterations with 10^7 packets each, shown by black circles and black points. The increased number of packets leaves the disk structure almost unchanged.

The spectrum of the radiation field in the gap is in figure 6. While most of the radiation lies in the peak corresponding to the disk's thermal emission, a significant minority (11% of the power) is in scattered starlight. A further fraction of a percent is absorbed and re-emitted by the disk, and subsequently scattered before reaching the gap (blue curve, right-hand end). The bolometric mean intensity of the radiation at the planet's orbit is 3.7% of that at the same location if the intervening disk material were removed.

The midplane temperature profiles from the six runs are plotted in figures 7 (for the three runs with star [A]) and 8 (star [B]). Despite the different surface density profiles of models [G] and [V], runs 2 and 3 have quite similar temperatures in the gap. The same is true of runs 5 and 6, where the temperatures are generally higher, due to the greater opacity
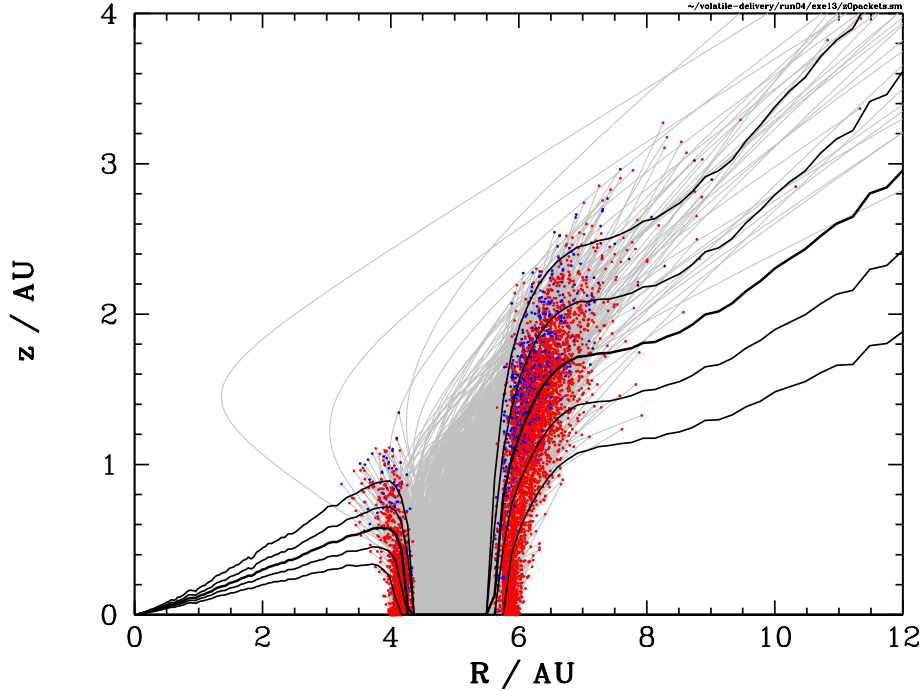
Fig. 5.— Paths of every tenth photon packet reaching the gap midplane in run 3. The number of packets plotted is 7613. Dots mark the locations of last interaction before crossing the midplane, and their colors show whether the packet was last absorbed (red) or scattered (blue). All packets carry equal energy. Black lines indicate the surfaces of vertical optical depth 0.01, 0.1, 1 (heavier line), 10 and 100 (top to bottom) at the stellar blackbody peak wavelength (0.65 μm).

of the dust at the shorter wavelengths emitted by the hotter star [B].

The grey shading in figures 7 and 8 indicates the temperature range where water ice is stable at the midplane density found in the run with the viscous disk [V]. The gaps reach temperatures well above the water sublimation thresholds in all four runs with gaps, as shown by the curves exiting the gray shaded regions. We took the dependence of the sublimation temperature vs. density from Pollack et al. (1994), choosing the case where water ice contains 52% of the available oxygen. Lower fractions of the oxygen locked up in the water would correspond to lower sublimation temperatures. In the gap center in model [V] the densities are less than the lowest value in the Pollack et al. table, 10^{-18} g cm^{-3}. Although the true sublimation temperature should be lower, we simply use the lowest tabulated value.

Heavy elements can be delivered to the planets trapped in ices, provided the material is kept at temperatures somewhat below the ice sublimation threshold (Lunine & Stevenson
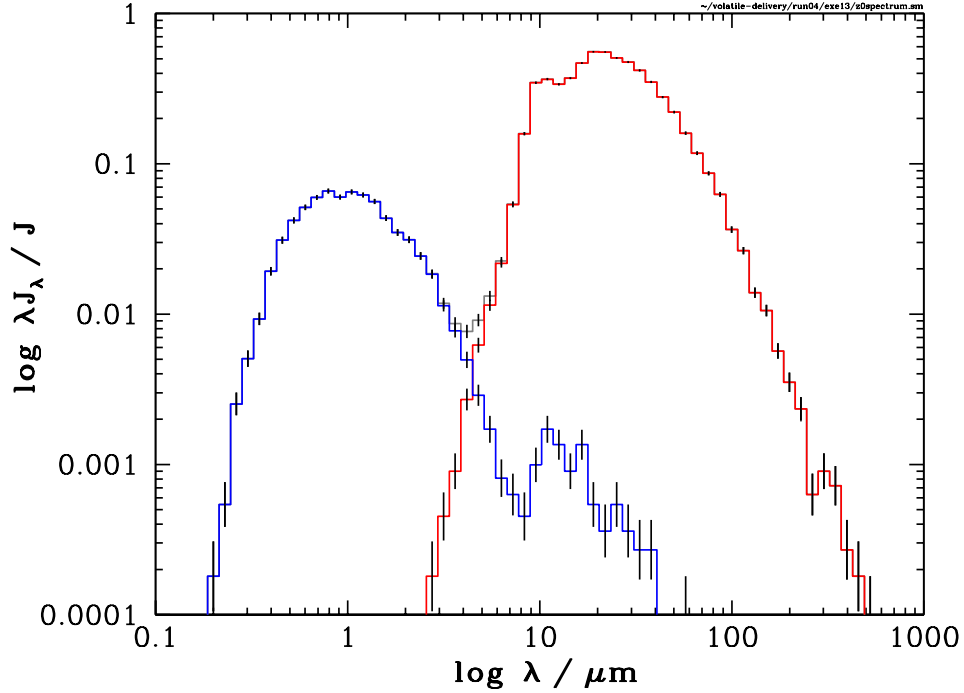
Fig. 6.— Spectrum of the radiation reaching the gap midplane in the same calculation shown in figure 5. The packets that most recently interacted by scattering (blue histogram) have a spectrum similar to the star, while the packets that were last absorbed and re-emitted (red) are at mid- to far-infrared wavelengths corresponding to the temperatures found in the disk. A weak silicate feature appears at 10-μm. The grey histogram visible only at intermediate wavelengths is the sum of the scattered and absorbed radiation. The vertical axis is the mean specific intensity J_λ as a fraction of the mean bolometric intensity J, multiplied by the wavelength so that equal areas correspond to equal luminosities. The resulting quantity is dimensionless. Error bars show the $\sqrt{N}$ uncertainties under Poisson statistics.

1985). In order to determine the heliocentric distance where trapping is effective, we calculate the stability curve of a mixed clathrate hydrate in equilibrium with the solar nebula, for two commonly-used determinations of the nebular elemental abundances (Anders & Grevesse 1989; Lodders 2003).

First, we apply empirical expressions fitted to experimental data from the literature to calculate the dissociation pressure $P_{d,i}$ as a function of temperature for the i species CH_4, CO_2, Xe (parameters from Fray et al. 2010), CO, N_2, H_2S, Ar, and Kr (parameters from Hersant et al. 2004). Then we use the method described in Mousis et al. (2009) to determine

the molar fractions y_i of each species in the gas phase, for elemental abundances taken from Anders & Grevesse (1989) and Lodders (2003). The stability curve of a mixed clathrate in equilibrium with the solar nebula is obtained by calculating the dissociation pressure at each temperature, $P_{d,mix}$ using the following equation (e.g. Miller 1974):

$$P_{d,mix} = \left(\sum_i \frac{y_i}{P_{d,i}} \right)^{-1} \tag{1}$$

The resulting stability curves are plotted in figure 9 along with the temperature-pressure profiles of three of our model solar nebulae. The stability curves for the two sets of elemental abundances are very similar, and both indicate clathrate hydrates are stable in the three nebulae at temperatures below 81 K found only outside 7.7 AU, well beyond the outer edge of the gap. Furthermore, these stability curves are extremely close to the stability curve of pure H_2S clathrates (not shown for legibility), which implies that clathrate hydrates forming under these conditions contain almost exclusively H_2S. Much colder temperatures, below about 50 K, must be attained for these clathrates to trap large amounts of Ar, Kr, Xe and N_2. Therefore, the volatile fraction of planetesimals that formed Jupiter needs to originate from heliocentric distances exceeding 20 AU to account for the heavy element enrichments measured by the Galileo spacecraft in the planet's atmosphere (e.g. Owen et al. 1999).

Finally, synthetic images of the run 3 model nebula, of the kind that might one day be obtained by pointing a large infrared interferometer at a protostellar disk in a nearby star-forming region, are shown in figure 10. The gap's outer edge is hot because it is both directly exposed to starlight, and more tilted toward the star than other parts of the disk. Furthermore, it is surrounded on the inside by the optically-thin dark gap and on the outside by disk annuli in shadow. As a result the gap's outer edge stands out as a bright ring. At wavelength 20 μm, near the peak of the local thermal emission, the face-on surface brightness contrast between the bright ring at 6.5 AU and the shadowed disk at 10 AU is a factor 23.

4. DISCUSSION

Below we discuss the robustness of the hot gap phenomenon, the distribution of the heating, the consequences for primitive bodies in and near the gap, and several scenarios for the volatile enrichment of Jupiter and its satellites.
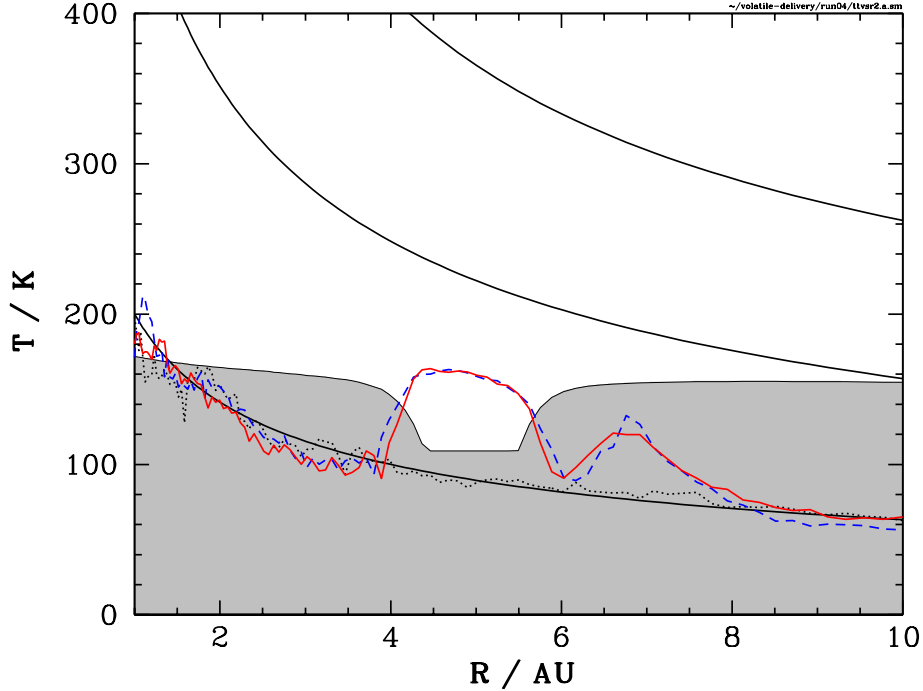
Fig. 7.— Midplane temperature vs. radius in the runs with star [A]. Dotted, dashed and solid lines show respectively runs 1, 2 and 3. Grey shading marks the region where water ice is stable at the midplane densities found in run 3. Solid black curves show for comparison the temperatures of (top to bottom) grains directly exposed to the starlight, blackbodies directly exposed to the starlight, and the initial condition for the radiative-hydrostatic iterations, $T = 200\,\mathrm{K}/R_{\mathrm{AU}}^{1/2}$.

4.1. Location and Extent of the Heating

The high Solar luminosity makes the whole nebula hotter than a T Tauri disk, even in the absence of any gaps. The temperature at Jupiter's orbit is high enough to destroy clathrate hydrates, at 88 to 100 K (table 1; figure 9). There will be consequences also for the stability of amorphous ice, whose presence near the giant planets has already been questioned (Kouchi et al. 1994; Gautier & Hersant 2005). With the potential carrier materials unstable, it will be difficult to form the planet in situ from material enriched in volatile-trapping ices.

Stars less luminous than $10L_\odot$ yield lower temperatures, but the gap remains above the water sublimation threshold even at $3L_\odot$, as we check using the following scaling. The flux of radiation heating the gap is proportional to the Solar luminosity L and to the disk thickness. The thickness in turn is proportional to the sound speed, which varies as the square root
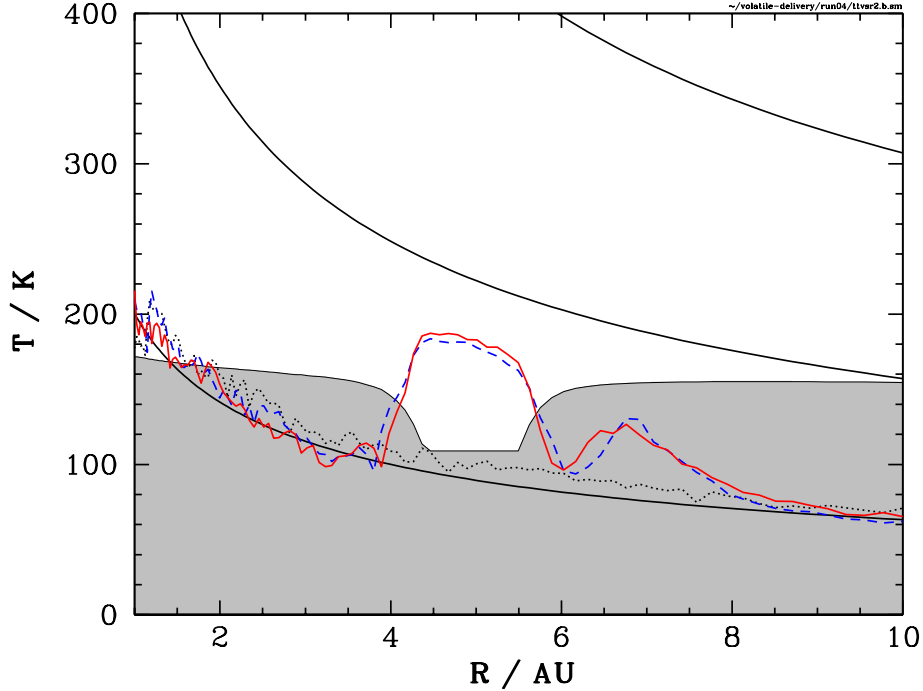
Fig. 8.— Same as figure 7 but for the runs 4, 5 and 6 with star [B]. The shorter wavelengths of the light emitted by the hotter star correspond to higher dust opacities, leading to a hotter gap than in figure 7. Temperatures are higher also for grains directly exposed to starlight (solid black curve at top right).

of the temperature. On the other hand, the radiative cooling rate of the material in the gap is proportional to T^4 times the Planck-mean absorption opacity κ_P. At temperatures near the sublimation threshold, $\kappa_P \sim T^{5/4}$ approximately. Balancing heating and cooling yields $T \sim L^{4/19}$, so reducing the luminosity from 10 to $3L_\odot$ should reduce the temperature from 159 to 123 K. This is close to the temperature of 124 K found at the planet's orbit, in a version of run 3 with the luminosity reduced to $3L_\odot$ by shrinking the stellar radius to $2.75R_\odot$. With the luminosity reduced further to $1L_\odot$ by shrinking the star to $1.59R_\odot$, the temperature of 101 K again is close to the scaling law estimate of 98 K.

Our temperatures are lower limits since we neglected both the luminosity of the protoplanet and the accretion luminosity of the nebula itself. We also neglected the contribution to the radiation field from the envelope of gas and dust surrounding and falling onto the nebula. Absorption by material along the line of sight from the star can reduce the flux reaching the disk, while reprocessing by material above the disk increases the flux (D'Alessio et al.
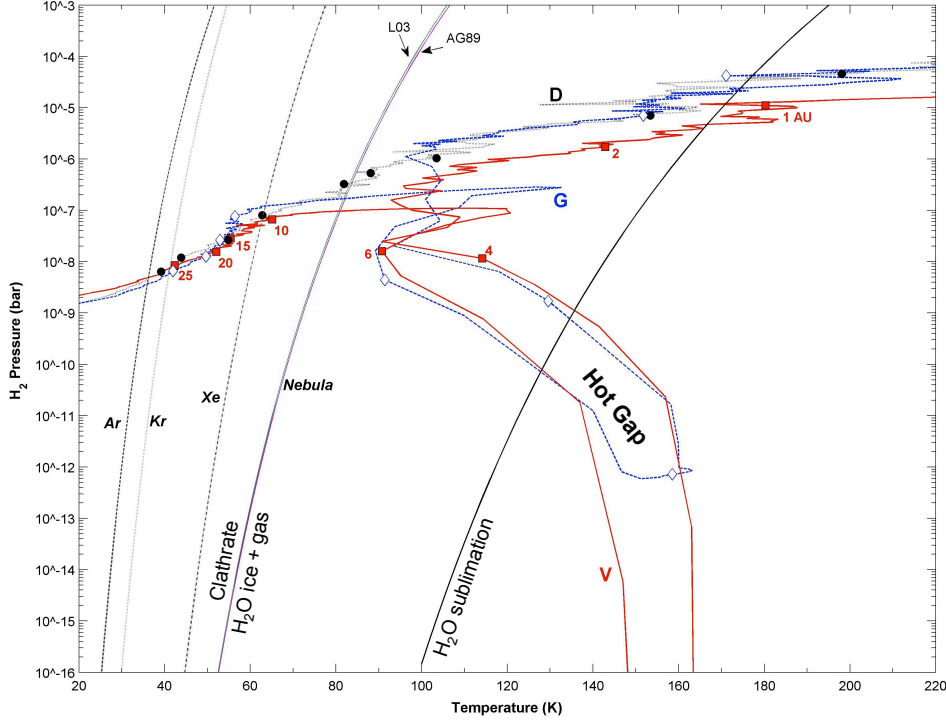
Fig. 9.— Pressure-temperature profiles of the three nebula models with star [A], compared against the sublimation curve of water ice and the stability curves of clathrate hydrates. As in previous figures, dotted, dashed and solid lines are for the models with disks [D], [G] and [V], respectively. Heliocentric distance markers are placed at 1, 2, 4, 5, 6, 10, 15, 20, and 25 AU. The curves are shown for pure argon, krypton and xenon clathrates, and for a mixed clathrate in equilibrium with the solar nebula for elemental abundances after Anders & Grevesse (1989) and Lodders (2003), labeled AG89 and L03 respectively. In all three models, clathrates are unstable at Jupiter and thus cannot readily deliver volatiles to the planet. Water ice sublimates easily in the two models with a gap.

1997). Estimating the net effect is a worthwhile goal for future work. We have neglected the anisotropy of the scattering, but that is unlikely to change the temperatures significantly because most of the photon packets reaching the planet's orbit were absorbed and re-emitted rather than scattered (figure 6).

The temperatures inside the gap are basically independent of the surface density, provided the gap is optically-thin in the vertical direction, as shown by the close match between the results with disks [G] and [V] (figures 7 and 8). The outcome is thus independent of the density floor chosen in model [G]. In the same vein, optically-thin non-axisymmetric wakes
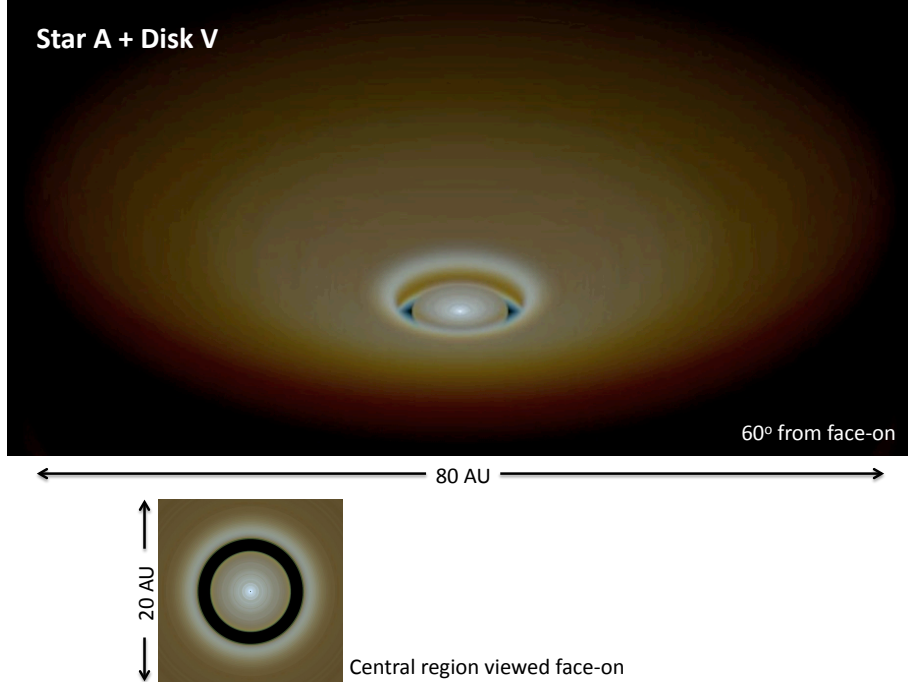
Fig. 10.— Synthetic images of run 3. The red, green and blue channels correspond to wavelengths 40, 20 and 10 μm. The intensity scale is logarithmic with the central protostar saturated. At top, the system is viewed $60°$ from face-on and the field of view is just over 80 AU across. The gap's outer rim is hotter than its surroundings and appears as a bright ring. Also visible through the gap is the hot rim on the disk's lower surface. The gap itself appears bluish because the sightlines pass through optically-thin hot material overlying the rings that emits most strongly at 10 μm. The bottom panel is a face-on view of the central 20 AU on the same color scale.

raised within the gap by the planet's tides are likely to have little effect on the heating. Unit optical depth corresponds to surface density a few tenths of a gram per square centimeter, considering the opacity (figure 3) at the radiation field's peak wavelength of 20 μm (figure 6). The temperatures also increase only slowly with height, being less than 3 degrees hotter at 0.05 AU above the planet. On the other hand, the outcome will depend on the gap width. The outer rim of a narrower gap will receive less direct sunlight, and re-radiate less power toward the equatorial plane.

The gap is optically-thin to the sunlight in the vertical direction between 4.33 and 5.68 AU in our run 3, while the temperatures computed by the Monte Carlo procedure exceed the local sublimation threshold from 4.17 to 5.62 AU. Note that the high temperatures extend

past the edge of the optically-thin region only on the gap's inner side, which more directly views the sunlit outer rim. The heated region includes the orbits of Jupiter's Trojan asteroids, the Thule group and the outer parts of the Hilda group. Any primordial populations in these locations will be thermally altered. It would be interesting to learn whether the planetesimal devolatilization associated with an early origin of Jupiter is compatible with the present makeup of the asteroid families, under standard scenarios for Solar system dynamical evolution such as the Nice model (Tsiganis et al. 2005).

Bodies trapped beyond the gap's outer rim also experience ambient temperatures high enough to affect volatile species. Temperatures near the local maximum in gas pressure, at 6.8 AU, are 120 to 133 K in the four models from table 1 with gaps, owing to the extra sunlight absorbed on the rim overhead. Gas drag forces push meter-sized bodies toward the pressure maximum (Bryden et al. 2000; Haghighipour & Boss 2003), where they can spend many orbits in warm surroundings. The temperatures and pressures are in the regime where water ice is stable but clathrate hydrates are not (figure 9). At the same location with no gap, the temperature is about 83 K and some of the clathrates are stable. In general there is a band at or beyond the planet's orbit where H_2S and xenon clathrates are stable, but argon clathrates are not. This is problematic since Jupiter is enriched in many volatile elements including sulfur, xenon and argon by similar factors of about 2.5 with respect to Solar (Young 2003).

Jupiter could have formed early but further from the star, where the temperatures were low enough for water ice and clathrates to be stable. In this scenario, the planet later migrated inward to its present position. We investigate the migration distance required using a pair of additional experiments. Star [A] illuminates a version of the viscous disk [V] with the planet moved to 10 AU in one case, and 20 AU in the other. The temperatures reached in the gap at the planet's orbit are 117 and 84 K, respectively. The first is above the water sublimation threshold, while the second allows stable water ice but destroys clathrate hydrates. Enriching Jupiter in heavy elements that were trapped in clathrates in and near the planet's gap was difficult during the early epoch we consider, unless the planet formed outside 20 AU.

Saturn too can be located in a hot gap, if its tides open a clearing in the nebula that is wide enough for a substantial area on the outer rim to be directly sunlit, and if the optical depth is sufficiently low for the reprocessed and scattered radiation to reach the planet. We evaluate the temperatures using a further run having star [A] and a version of disk [V] in which a single Saturn-mass planet orbits at 10 AU. Due to its lower mass, Saturn opens a gap almost three times narrower than run 3 in relative terms, with the outer radius at unit vertical optical depth only 11% greater than the inner. The gap also has weaker surface

density contrast and, although still quite optically thin to its own thermal emission, is only marginally optically thin for photons at the stellar blackbody peak, with an optical depth of 0.18 at the planet's orbit. The resulting temperature is 100 K, well below the value of 117 K obtained with Jupiter at the same location. Water ice is then stable, but clathrates decompose.

4.2.   Enriching Jupiter in Volatiles

Jupiter can potentially form directly from material enriched in heavy elements in a gravitationally unstable Solar nebula. The nebula develops spiral arms where gas drag forces concentrate meter-sized solid bodies (Rice et al. 2004). The planets form in part from the arms and so receive extra boulder-sized material compared to the nearby nebula (Boley & Durisen 2010). However we have seen that temperatures even in the optically-thick early nebula are high enough to make volatile-trapping ices unstable (section 4.1). It will be difficult to form Jupiter at 5 AU directly from material enriched in volatile elements such as the noble gases.

As the planet nears its final mass, its tidal forces become capable of opening a hot gap. However, bringing the tides into balance with the nebula's accretion stresses takes a few 10^4-year accretion timescales across the gap width, much longer than the 10^3-year timescale for growing the planet by gravitational collapse (Boss 1997). The gap will therefore clear only after Jupiter receives nearly all its mass. If the planet is not yet enriched on reaching this stage, newly added material must be more and more depleted in hydrogen and helium in order to produce the final abundances. Once it becomes insufficient to accrete nebular gas mixed with the vapors from sublimated volatile ices, the last viable route to enrichment is by accreting the solid icy bodies themselves.

The impact of the hot gap on icy bodies in Jupiter's vicinity depends on the bodies' sizes:

1. Bodies small enough to sublimate within the minimum gap-crossing time (about one orbital period or 10 yr) lose their clathrates, gas-laden amorphous ice, and other volatiles, and cannot deliver noble gases. The largest solid icy body that sublimates completely on this timescale at temperature 160 K is about 10 cm, using the sublimation law from Sack & Baragiola (1993). Smaller bodies lose their clathrates, gas-laden amorphous ice, and other volatiles, and cannot deliver noble gases.

2. Somewhat bigger icy bodies heat to the ambient temperature within the minimum gap-crossing time but do not completely sublimate. The smallest body capable of keeping

a cool center during the gap-crossing is 10 m, using 0.01 cm^2 s^{-1} for the thermal diffusivity of water ice.

3. Larger planetesimals could preserve volatiles. Bigger bodies' internal temperatures remain below the clathrate loss threshold for at least an orbital period when exposed to the gap. These bodies can deliver noble gases to Jupiter if they reach the planet fast enough. However, icy planetesimals that remain in the gap for extended time periods eventually vaporize unless their ice is shielded by the development of a lag deposit. This can be achieved if the regolith reaches a depth of a few hundred meters (Fanale & Salvail 1989; Schorghofer 2008).

Dynamics impose an additional constraint on the sizes of the bodies reaching the planet. Bodies larger than a meter can be trapped in outer mean-motion resonances with the planet (Weidenschilling & Davis 1985), while particles of centimeter to meter size are pushed away from the planet's orbit by gas drag forces. The bodies most easily accreted are grains smaller than 10 μm, which are swept in with accreting gas (Paardekooper 2007). If applied together, the dynamical and thermodynamical constraints prevent all enrichment in volatiles with respect to the nearby Solar nebula: only small particles approach the planet, and these quickly vaporize.

The hot gap also illuminates the circumjovian nebula, raising temperatures to levels that may impact the chemistry of the forming Jovian satellites. Growing Ganymede requires conditions appropriate for the condensation of water ice (Lunine et al. 2010), well below the temperature floor imposed by the radiation bathing the planet's environment in the hot gap. The circumplanetary material will reach temperatures similar to those listed in table 1 whether optically-thick (Mosqueira & Estrada 2003) or thin (Canup & Ward 2002). Our findings thus indicate that an early satellite formation epoch is inconsistent with the Ganymede temperature constraint. In any case, it has been suggested that the Galilean satellites correspond to a late generation of moons formed around the time the Solar nebula dispersed (Canup & Ward 2006; Barr & Canup 2008), several million years after the hot gap event.

5. Conclusions

We used a Monte Carlo radiative transfer approach to compute temperatures in the Solar nebula during the early epoch when the Sun was ten times more luminous than today. The midplane around 5 AU was hot enough to destroy clathrate hydrates, even with the nebula optically-thick, pointing to difficulties in forming Jupiter in situ directly from material

enriched in volatiles such as the noble gases.

If the planet nevertheless approached its final mass within a few hundred thousand years of the Sun, opening an optically-thin gap in the Solar nebula, then enough sunlight was reprocessed and scattered into the gap to heat the gas and dust to temperatures above 150 K that caused the loss of water and other volatiles from incoming small bodies, slowing or stopping the enrichment of the planet in heavy elements with respect to its surroundings.

An early origin may still be possible, if Jupiter either (1) formed much further from the Sun, and was enriched before migrating inward, or (2) was enriched in heavy elements and acquired its icy satellites only later, after the Sun became less luminous. In the first case, Jupiter would need to form beyond 20 AU in the particular model we considered, to enable the delivery of clathrate hydrates bearing the noble gases. In the second case, the enrichment must occur after the Sun has dimmed below $3L_\odot$, by which time the planet's cooling and contraction can greatly reduce its cross-section for capturing planetesimals (Helled & Bodenheimer 2011).

More generally, our results demonstrate that the Sun's luminosity is a parameter worth accounting for in any model of the formation of volatile-rich bodies.

REFERENCES

Anders, E., & Grevesse, N. 1989, Geochim. Cosmochim. Acta, 53, 197

Andrews, S. M., Wilner, D. J., Hughes, A. M., Qi, C., & Dullemond, C. P. 2010, ApJ, 723, 1241

Barr, A. C., & Canup, R. M. 2008, Icarus, 198, 163

Bell, K. R., & Lin, D. N. C. 1994, ApJ, 427, 987

Binney, J., & Tremaine, S. 1987, Galactic dynamics (Princeton, NJ, Princeton University Press)

Bjorkman, J. E., & Wood, K. 2001, ApJ, 554, 615

Boley, A. C., & Durisen, R. H. 2010, ApJ, 724, 618

Bolton, S. J. 2010, in IAU Symposium, Vol. 269, IAU Symposium, 92–100

Boss, A. P. 1997, Science, 276, 1836

Bryden, G., Różyczka, M., Lin, D. N. C., & Bodenheimer, P. 2000, ApJ, 540, 1091

Cai, K., Pickett, M. K., Durisen, R. H., & Milne, A. M. 2010, ApJ, 716, L176

Canup, R. M., & Ward, W. R. 2002, AJ, 124, 3404

—. 2006, Nature, 441, 834

D'Alessio, P., Calvet, N., & Hartmann, L. 1997, ApJ, 474, 397

D'Antona, F., & Mazzitelli, I. 1994, ApJS, 90, 467

Dodson-Robinson, S. E., Veras, D., Ford, E. B., & Beichman, C. A. 2009a, ApJ, 707, 79

Dodson-Robinson, S. E., Willacy, K., Bodenheimer, P., Turner, N. J., & Beichman, C. A. 2009b, Icarus, 200, 672

Doppmann, G. W., Greene, T. P., Covey, K. R., & Lada, C. J. 2005, AJ, 130, 1145

Dullemond, C. P., Hollenbach, D., Kamp, I., & D'Alessio, P. 2007, Protostars and Planets V, 555

Durisen, R. H., Boss, A. P., Mayer, L., Nelson, A. F., Quinn, T., & Rice, W. K. M. 2007, Protostars and Planets V, 607

Evans, II, N. J., et al. 2009, ApJS, 181, 321

Fanale, F. P., & Salvail, J. R. 1989, Icarus, 82, 97

Fray, N., Marboeuf, U., Brissaud, O., & Schmitt, B. 2010, J. Chem. Eng. Data, 55, 5101

Gautier, D., & Hersant, F. 2005, Space Sci. Rev., 116, 25

Greene, T. P., & Lada, C. J. 2002, AJ, 124, 2185

Haghighipour, N., & Boss, A. P. 2003, ApJ, 583, 996

Hartmann, L., Cassen, P., & Kenyon, S. J. 1997, ApJ, 475, 770

Hartmann, L., Zhu, Z., & Calvet, N. 2011, ArXiv e-prints

Hayashi, C. 1961, PASJ, 13, 450

Helled, R., & Bodenheimer, P. 2011, Icarus, 211, 939

Helled, R., & Schubert, G. 2009, ApJ, 697, 1256

Hersant, F., Gautier, D., & Lunine, J. I. 2004, Planet. Space Sci., 52, 623

Hirose, S., & Turner, N. J. 2011, ApJ, 732, L30+

Hosokawa, T., Offner, S. S. R., & Krumholz, M. R. 2011, ApJ, 738, 140

Hubickyj, O., Bodenheimer, P., & Lissauer, J. J. 2005, Icarus, 179, 415

Kouchi, A., Yamamoto, T., Kozasa, T., Kuroda, T., & Greenberg, J. M. 1994, A&A, 290, 1009

Lin, D. N. C., & Papaloizou, J. 1986, ApJ, 307, 395

Lin, D. N. C., & Papaloizou, J. C. B. 1993, in Protostars and Planets III, ed. E. H. Levy & J. I. Lunine, 749–835

Lodders, K. 2003, ApJ, 591, 1220

Lubow, S. H., & D'Angelo, G. 2006, ApJ, 641, 526

Lucy, L. B. 1999, A&A, 344, 282

Lunine, J., Choukroun, M., Stevenson, D., & Tobie, G. 2010, The Origin and Evolution of Titan, ed. Brown, R. H., Lebreton, J.-P., & Waite, J. H. (Springer Science+Business Media B.V.), 35–+

Lunine, J. I., & Stevenson, D. J. 1985, ApJS, 58, 493

Miller, S. L. 1974, in Natural Gas in Marine Sediments, ed. I. R. Kaplan (New York: Plenum), 151–177

Mosqueira, I., & Estrada, P. R. 2003, Icarus, 163, 198

Mousis, O., Marboeuf, U., Lunine, J. I., Alibert, Y., Fletcher, L. N., Orton, G. S., Pauzat, F., & Ellinger, Y. 2009, ApJ, 696, 1348

Movshovitz, N., Bodenheimer, P., Podolak, M., & Lissauer, J. J. 2010, Icarus, 209, 616

Nisini, B., Antoniucci, S., Giannini, T., & Lorenzetti, D. 2005, A&A, 429, 543

Owen, T., Mahaffy, P., Niemann, H. B., Atreya, S., Donahue, T., Bar-Nun, A., & de Pater, I. 1999, Nature, 402, 269

Paardekooper, S.-J. 2007, A&A, 462, 355

Pollack, J. B., Hollenbach, D., Beckwith, S., Simonelli, D. P., Roush, T., & Fong, W. 1994, ApJ, 421, 615

Pollack, J. B., Hubickyj, O., Bodenheimer, P., Lissauer, J. J., Podolak, M., & Greenzweig, Y. 1996, Icarus, 124, 62

Preibisch, T., Ossenkopf, V., Yorke, H. W., & Henning, T. 1993, A&A, 279, 577

Rice, W. K. M., Lodato, G., Pringle, J. E., Armitage, P. J., & Bonnell, I. A. 2004, MNRAS, 355, 543

Sack, N. J., & Baragiola, R. A. 1993, Phys. Rev. B, 48, 9973

Sato, B., et al. 2005, ApJ, 633, 465

Schorghofer, N. 2008, ApJ, 682, 697

Siess, L., Dufour, E., & Forestini, M. 2000, A&A, 358, 593

Toomre, A. 1964, ApJ, 139, 1217

Tsiganis, K., Gomes, R., Morbidelli, A., & Levison, H. F. 2005, Nature, 435, 459

Varnière, P., Bjorkman, J. E., Frank, A., Quillen, A. C., Carciofi, A. C., Whitney, B. A., & Wood, K. 2006, ApJ, 637, L125

Weidenschilling, S. J., & Cuzzi, J. N. 1993, in Protostars and Planets III, ed. E. H. Levy & J. I. Lunine, 1031–1060

Weidenschilling, S. J., & Davis, D. R. 1985, Icarus, 62, 16

Young, R. E. 2003, New A Rev., 47, 1